Composites: Part A 177 (2024) 107955

Contents lists available at ScienceDirect

Composites Part A

journal homepage: www.elsevier.com/locate/compositesa

On the understanding of bubble dynamics through a calibrated textile-like porous medium using a machine learning based algorithm

João Machado [a], Masoud Bodaghi [b,*], Mostafa Nikzad [c], Pedro P. Camanho [a], Suresh Advani [d], Nuno Correia [a]

[a] Institute of Science and Innovation in Mechanical and Industrial Engineering, Porto, Portugal
[b] Luxembourg Institute of Science and Technology (LIST), 5, rue Bommel | L-4940, Hautcharage, Luxembourg
[c] Faculty of Science, Engineering and Technology, Swinburne University of Technology, Hawthorn, Victoria 3122, Australia
[d] Center for Composite Materials and Department of Mechanical Engineering, University of Delaware, United States

ARTICLE INFO

Keywords:
E: Liquid Composite Moulding
B: Defects
E: 3-D Printing
B: Porosity
B: Permeability

ABSTRACT

In this work, we present a proof of concept for both 3D-printed media and a machine learning analysis methodology to investigate void formation and transport during liquid filling. Through a series of experiments, we characterized void formation and transport at constant flow rates using two calibrated fabric-like porous geometries created by Stereolithography and Multi Jet Fusion 3D printing techniques. Our findings highlight the significance of porous medium geometry and void size, in addition to the capillary number, in characterizing void formation and mobility during resin flow into a mold containing a fibrous preform. Notably, the paper's strength lies in the presentation of advanced bubble analysis methods, including frame-by-frame high-resolution video analysis, enabling the identification of individual bubbles and the extraction of their statistics, such as count, size, and velocity throughout the experiment. These insights contribute to the design of more efficient processes, resulting in composite parts with reduced void content.

1. Introduction

In Liquid Composite Moulding (LCM) process, after placing a dry textile preform in a sealed mould cavity, a pressure differential is imposed, either by vacuum, or using positive pressure. This pressure differential is what drives the resin flow inside the mould cavity, permeating and saturating the fibrous preform. Usually, lower viscosity polymeric resins are used in LCM (with viscosities in the range of 1 to 100 mPa.s), as these facilitate the fibrous reinforcement impregnation process [1 2]. Resin Transfer Moulding (RTM), Vacuum-Assisted RTM (VARTM), and Vacuum Infusion (VI) are some of the processes that belong to the family of LCM [34]. Experience with the LCM technology family has demonstrated that it is possible to manufacture aircraft components such as the co-cured [5], MRJ empennage box structure [6] and automotive components such as doors, roofs, and side panels with comparable quality to those of an autoclave [7].

During the LCM process, the resin that impregnates the preform may contain bubbles or dissolved air or volatiles that will manifest into bubbles during the mould filling process.

Also, air pockets may form when two flow fronts meet and result in bubbles. If during the filling process, the bubbles don't reach a vent they are entrapped in the composite and become voids in the matrix after the resin cures. This phenomenon is crucial to understand, as it directly impacts the quality and integrity of the final composite material. On the other hand, transport mechanisms refer to the movement of bubbles within the flowing resin. This primarily encompasses the advection of bubbles due to resin flow and the motion of individual air molecules within the resin [8–10]. While these mechanisms indeed play a significant role, the primary objective in the LCM processes is to investigate the initial formation of voids at the flow front, as this stage holds paramount importance in determining the overall void structure. The autoclave process operates under different conditions and involves distinct mechanisms (resin flow is minimal) [11].

Voids have a detrimental impact on the mechanical properties of composite parts [12]. This poses a reliability concern in the design of composite parts especially for high performance industrial cases, such as the ones used in aerospace applications. In addition, literature points out that despite global void content being an important indicator, the actual

* Corresponding author.
E-mail address: masoud.bodaghi@list.lu (M. Bodaghi).

https://doi.org/10.1016/j.compositesa.2023.107955
Received 24 July 2023; Received in revised form 1 December 2023; Accepted 6 December 2023
Available online 9 December 2023
1359-835X/

shape, size and distribution of voids have a significant impact on the final mechanical performance of the composite part [12–15]. Hence, understanding void formation mechanisms as well as its dynamics and applying proper resin impregnation strategies for void elimination have been the topic of key interest to researchers for the last two decades. From a macroscopic point-of-view, the preform impregnation process can be modelled using Darcy's law [16], which states that the volume average flow velocity $\vec{u}$ is dependent on the pressure gradient ∇p, the fluid viscosity μ, and the permeability tensor of the porous medium $\boldsymbol{K}$:

$$\vec{u} = -\frac{\boldsymbol{K}}{\mu}\nabla \mathrm{p} \tag{1}$$

$$\nabla . \vec{u} = 0 \tag{2}$$

By coupling Darcy's law (Eq. (1)) with the continuity equation (Eq. (2)), it is possible to numerically solve LCM mould filling problems, therefore predicting possible locations of insufficient preform impregnation [17].

The goal in LCM is to fill all the empty porous spaces with resin before it cures. In a textile preform, the empty porous spaces range from nanometres to a few micrometres in between fibres, forming the microscale porosity (intra-tow porosity). On the other hand, the spaces in between fibre tows, with a typical width of 80–250 μm, form the mesoscale porosity (inter-tow porosity) [18]. In turn, this dual-scale porosity of the textile preform induces different flow rates, present in the inter-tow and intra-tow pore zones.

The imbalance of flow rates between micro and *meso*-scales forms a fingering effect or saturation lead-lag flow, and hence leads to void formation by air encapsulation. Inter-tow voids form between the tow channels and intra-tow voids form inside the tow. The formation of voids inside the composite part can be described by competition between the viscous and the capillary forces, as the flow between the tows is mainly governed by the viscous forces while, the flow inside the tows is dominated by capillary forces [19].

This competition between viscous and capillary forces can be quantified in a dimensionless form by the capillary number, which relates the viscous forces to the surface tension forces acting across the resin-air interface (Eq. (3)):

$$Ca = \frac{v\mu}{\sigma} \tag{3}$$

where v is the volume average velocity, μ is the fluid viscosity and σ is the fluid surface tension.

Experimental studies refer to the capillary number as an important parameter in void dynamics. Regarding void formation, several studies report that there is an optimal capillary number that minimizes void formation during mould filling. This is attributed to the balancing of the contribution of the viscous and capillary forces present in the meso and micro scales, which even out the flow front profile, therefore minimizing lead-lag flow. Rohatghi *et al.* [20] found the optimum *Ca* to be on the order of 10^{-1}–10^{-2} for a unidirectional stitched fibre glass mat being impregnated by silicone and DOP oil. Zingraff et al. [21] found the optimum *Ca* value to be around 0.004–0.006 for a low-viscosity reactive thermoplastic resin. An optimum *Ca* value of 0.008 was reported by Leclerc and Ruiz [22] for a glass fibre woven fabric impregnated by a vinylester resin. Finally, after a literature review, Park and Lee [19] concluded that the optimum Ca value should be approximately 10^{-3}, translating to a resin velocity in the range of 0.1–1 mm/s.

As void formation during resin injection can only be minimized to a certain positive value above zero, research has also focused on characterizing what conditions may favour the mobilization of voids, with the end goal of purging the remaining voids, after mould filling. Rohatgi *et al.* have reported that intra-tow voids are much more difficult to purge than inter-tow voids [20], although no quantitative measure was presented. Due to difficulty in direct visualization of void transport phenomena in real fibrous reinforcements, a significant portion of research involves the experimental study in idealized porous structures, such as constricted capillary tubes [23 24], T-shaped junction devices [25] and pore doublet models (PDM) consisting of two connected capillaries [2627]. Nevertheless, these porous structure representations imply many simplifications to the actual porous structure of a dual scale porous medium, which in turn may not adequately represent the two-phase flow of resin and air commonly encountered in LCM fibrous reinforcements. While these setups offer practical advantages, they do impose limitations, particularly due to their confinement to one-dimensional flow.

As suggested by previous studies [28], besides the fluid flow mean velocity and fluid properties, the porous medium architecture should also play a major role in the degree of mobility of bubbles. Despite the considerable efforts of researchers, as emphasized in [29], effectively accurate experimental observation of bubble creation and migration in fibrous porous media remains a significant challenge in composites processing science.The non-uniformity of the flow channels encountered in reinforcements may entrap voids or hinder its average velocity, due to the added resistance in the cross-section constricted zones. As such, it is fundamental to have a detailed description of the porous structure, to carry out quantitative analyses on the effect of process parameters on void formation and transport. Still, it is difficult to obtain microstructural descriptions of an actual textile reinforcement, due to the stochastic nature and high variability of its porous structure [1830].

Motivated by the relevance of this subject, this study aims to evaluate the effect of flow conditions on void formation and transport inside a model porous media. To achieve this, a series of experiments were conducted using an idealized porous medium geometry already benchmarked in permeability tests [31], as means of reducing the porosity scatter observed in textile reinforcements. Moreover, the use of the cited porous medium geometry also allowed one to conduct the experimental void formation and transport analysis at a *meso*-scale level without addressing the macro and micro scales. This strategy aims to further decrease results uncertainty, as the statistical scatter observed in the macro and micro scales is eliminated. In this study, we present new insights and observations about the factors that influence void formation and their flow dynamics and mobility within a model and idealized porous medium.

Regarding the geometrical complexity of our model, we acknowledge the importance of achieving a high degree of similarity between the model and the actual medium it seeks to replicate. Real world scenarios are complex with multiple mechanisms at play which makes it difficult to study them and address their interaction in a meaningful way. In our study, we opted for a simplified model geometry for several reasons. Firstly, it provided us with a level of control over porosity variability that would have been challenging to attain with a real dual-scale fabric. This control was pivotal to enable us to systematically investigate the effects of porosity on void formation and transport, a critical aspect in liquid composite molding. Secondly, the chosen geometry facilitated a clear visualization of bubbles within the porous medium, which is often a challenging feat in more complex structures. It's important to note that this decision was not taken lightly; it was preceded by a series of meticulous iterations and comprehensive experimental studies which led to the selection of this representative and applicable porous media geometry.

2. Experimental setup and methodology

In our pursuit to delve into void dynamics at the *meso*-scale, we deliberately decoupled our analysis from micro-scale void dynamics and potential micro-meso scale interactions. This strategic choice was made to eliminate the complexities and potential confounding effects associated with interactions across multiple scales. By focusing exclusively on the *meso*-scale, we aimed to capture the natural variability of void formation and transport phenomena, unperturbed by inter-scale interactions. The proposed method in this study facilitated an

investigation into the effect of two-dimensional flow conditions which is prevalent in liquid composite molding processes. This enabled us to observe phenomena such as void entrapment, shedding light on critical aspects of void migration in porous media.

2.1. Calibrated textile-like porous medium

In this study, two textile-like porous networks with anisotropic permeability were manufactured by 3D printing techniques [31], using two different technologies, namely Stereolithography (SLA) and Multi Jet Fusion (MJF). These techniques provide very good geometrical accuracy, which enables a close control of the architecture of the porous medium, while the surface finish of the fabricated porous medium from SLA and MJF are distinctly different [32].

The 3D printed techniques allowed the manufacturing of the porous media without all of the sources of variability, inherent to real fabrics [31]. The porous medium possesses different resistances to flow in the two principal directions, as the porous gaps are wider in the Y direction (2.06 mm) than in the X direction (0.76 mm), as depicted in Fig. 1.

Both directions are considered in the flow experiments using the MJF printed porous medium, as means to evaluate the influence of the porous architecture on void formation and transport. Hereby, flow experiments in the direction of the smaller porous gaps (X direction) are designated "MJF small gap", whereas experiments in the larger gap direction (Y direction) are designated "MJF large gap". With the SLA printed porous medium, experiments were only conducted along the smaller gap direction.

The use of a benchmarked 3D printed model geometry instead of a real fabric will reduce the scatter and uncertainty and allow one to focus on one mechanism of void formation and transport. Therefore, by knowing the exact morphology of the porous medium, correlations between observed results and experimental parameters are easier to establish. The precise geometry of the 3D printed porous medium architecture further reduces scatter in results due to varying channel gaps, fiber tows and fiber volume fraction. The gap dimensions and geometry in the current study may deviate from those encountered in composite reinforcement processes. Nonetheless, the strategic intent was to establish a simplified model geometry to glean insights into the mechanisms of bubble formation and mobility. These mechanisms exhibit similarities that can be quantified using dimensionless numbers, accounting for the gap dimensions. However, Darcy's law is still valid in this porous medium geometry, as reported and confirmed by the permeability measurements in [31].

2.2. Flow experiments and visualization

The setup is designed to conduct rectilinear flow experiments, allowing the visual monitoring of the flow front and the air bubbles inside, as depicted in Fig. 2. The mould consists of a metallic frame with a top PMMA thick plate, which provides a rigid and leak free cavity to contain the porous medium. The test fluid is injected inside the mould with a controlled flow rate, ranging from 10 g/min to 100 g/min, using an Isojet® pump system. Each experiment was run at a constant flow-rate. A single inlet and outlet are provided in the mould. The test fluid used is a motor oil, with the properties provided in Table 1. Finally, a camera positioned above the mould allows the recoding of each experiment for data processing using an image analysis algorithm described below.

Each experiment is conducted at room temperature and starts with the opening of the inlet through which the test-fluid flows at a constant

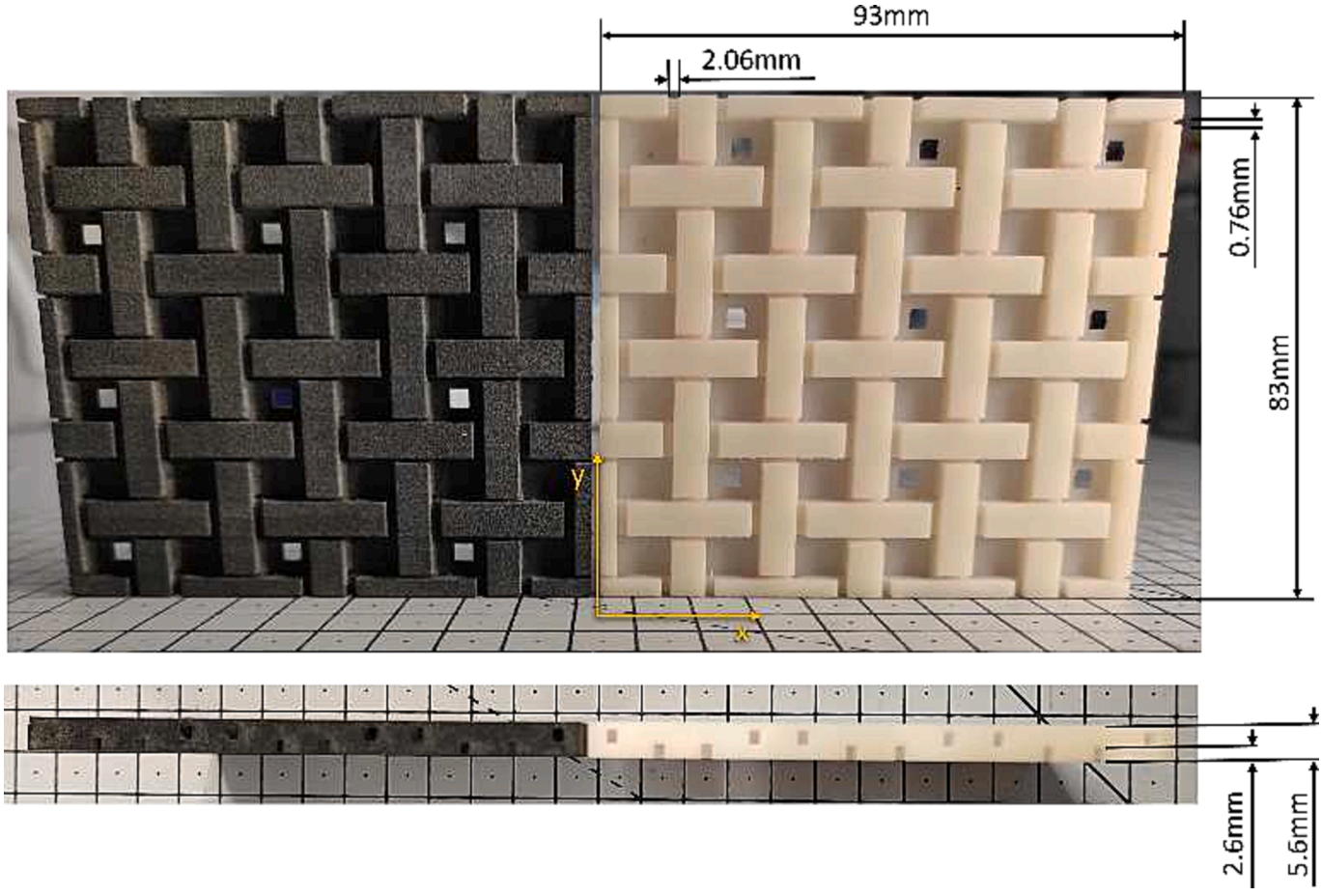

Fig. 1. Gaps dimensions of the 3D printed porous medium, according to axis orientation.

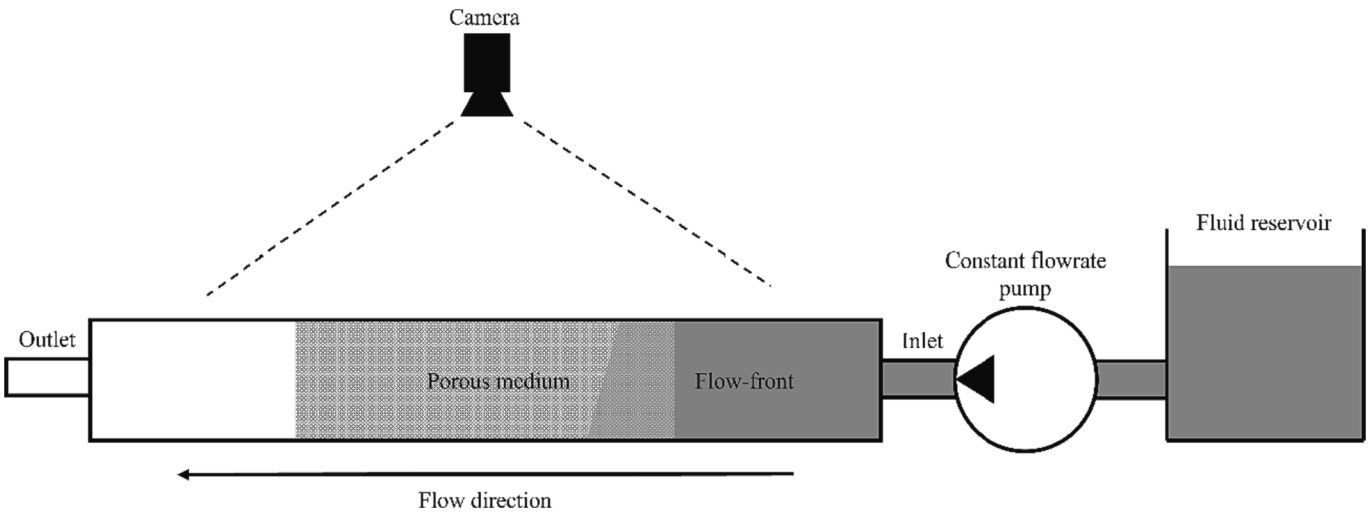

Fig. 2. Side view of experimental setup schematic.

Table 1
Rheological properties of the test fluid at room temperature.

Viscosity [mPa.s]	Density [kg/m^3]	Surface tension [mN/m]
71.4	875	33

flow rate. The bubbles are generated naturally with the flow-front progression within the porous medium, as depicted in Fig. 3. This happens due to mechanical air entrapment by the fluid flow, as there is a fingering effect analogous to the one observable in LCM processing. The experiments are terminated when the resin flow-front exits the porous medium, as the objective of this study is the analysis of void dynamics during the unsteady two-phase flow regime.

Using the fluid properties described in Table 1, the maximum experimental fluid flow velocity of 13.7 mm/s and the largest

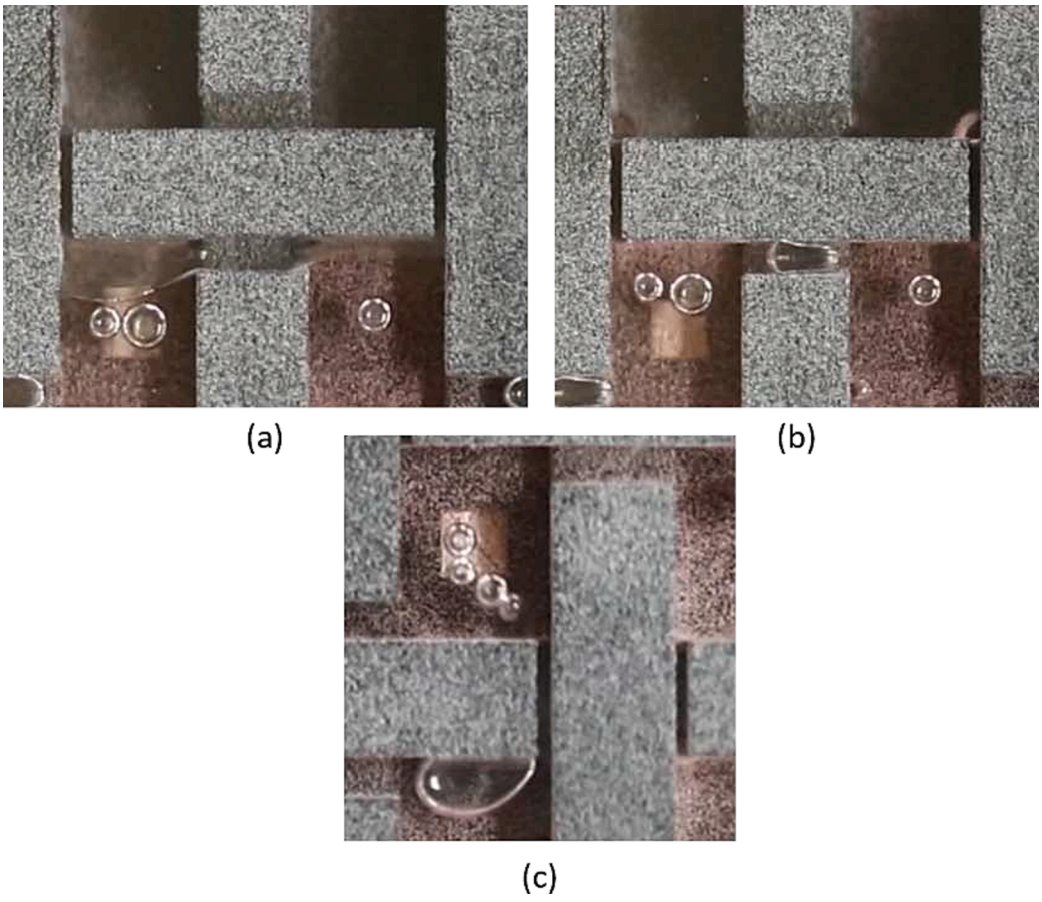

Fig. 3. Experimental visualization of different bubble behaviours: flow-front unification (a) leading to a bubble formed by flow-front mechanical air encapsulation (b); Bubble splitting leading to a train of smaller bubbles (c).

characteristic length of the porous medium, given by the hydraulic diameter of the largest channels (2.9 mm), the largest Reynolds number found is 0.38. As the Reynolds number is well below unity, it is reasonable to assume that the experimental fluid flow conditions represent creeping flow and are representative to those found in LCM processing [31,33].

2.3. Image processing algorithm

The algorithm responsible for processing relevant flow data is divided in three main modules: video frame acquisition and segmentation, bubble and flow-front tracking, velocimetry, and data post-processing [34].

The analysis is conducted on a frame-by-frame basis, using a recorded video of an experiment. To allow the extraction of bubble and flow-front data by the algorithm, each frame is firstly segmented using a U-Net convolutional neural network model [35] developed in TensorFlow [36] and trained for this specific purpose. The segmentation output encompasses four different classes: flow-front, bubble edge, bubble centre and the background (Fig. 4 (b)). In each frame, three geometric parameters are calculated for each bubble: its centroid position, area, and the perimeter. These properties are calculated using contour-based approaches, the methods of which are provided in the OpenCV library [37]. To ensure that the measured properties are assigned to the correct bubble, a unique label is attributed to each newly detected bubble (visible in Fig. 5). As such, when the parsing of the video is complete, each bubble will have its own property history record. The tracking of each individual bubble throughout the video recording is achieved using the fDSST correlation tracker for each bubble centre contour (which implementation is available in the Dlib library [38]). The tracking of the flow-front position throughout the flow experiment video recording is accomplished by computing the extreme point of the flow-front segmented class contour. This enables the calculation of the apparent fluid flow velocity inside the porous medium.

Fig. 4.

Regarding bubble and flow front velocity calculation, instead of calculating the velocities on each subsequent pair of frames, the average velocity was instead calculated in three equidistant sections of the frame (as depicted in Fig. 5), having the position history record of each bubble and the flow front. This approach avoids an extensive amount of noise in the velocity–time profiles of the bubbles and flow front, which is created when calculating the velocity on a frame-by-frame basis. Nevertheless, it provides sufficient detail to encompass eventual variations in the instantaneous flow front velocity, relative to the bubble velocity.

As the number of frames per second of the video is known *a priori*, the velocity of each bubble inside each section is calculated from the difference of the first and the last known positions of the bubble centroid in each frame section, divided by the time between reference frames, as shown in Eq. (4).

$$v_{sec} = \frac{x_1 - x_0}{n\frac{1}{FPS}} \tag{4}$$

Where x_1 and x_0 are the final and first known bubble or flow front positions on the frame segment respectively, n is the number of frames between the first and last known positions and FPS is the number of frames per second of the video capture. The mean bubble velocity is then calculated as the mean value of the different bubble section velocities (Eq. (5)). v_{sec} is the bubble velocity in each section of the porous medium and n_{sec} is the number of sections where the bubble was detected, as it may not be present in all the sections. It is important to note that in this study only the bubble velocity component that is parallel to the principal volume average apparent flow velocity was used, so that both bubble and flow front velocity are scalars.

$$v = \frac{1}{n_{sec}} \sum v_{sec} \tag{5}$$

2.4. Uncertainty analysis

The accuracy of the acquired data is crucial to conduct a reliable post-processing analysis, such as the one described in the former section. Image resolution plays a significant role in the detection of the bubble shape, by the artificial vision algorithm, which subsequently affects the bubble size and motion parameters. All videos were recorded with a resolution of 1280x720 pixels at 50 frames per second. The camera was positioned perpendicular to the experiment field of view, at a distance that ensured that the porous medium length was visible in the video frame.

A study on the algorithm's accuracy was conducted prior to the experimental recordings analysis, using a validation dataset composed by frames randomly extracted from experiment recordings. It was found that the mean error values in bubble area computation led to an over-prediction of 7.3 % using the SLA printed porous medium and 13.8 % using the MJF printed porous medium. These differences are believed to be due to the underlying visual aspect of the porous media, as the differences in surface roughness and material colours can interfere with the contrast between the bubble and the fluid regions.

Since velocity data is calculated considering the first and last bubble centre of mass positions in each section of the porous medium, it was found that the uncertainty regarding the bubble centre of mass

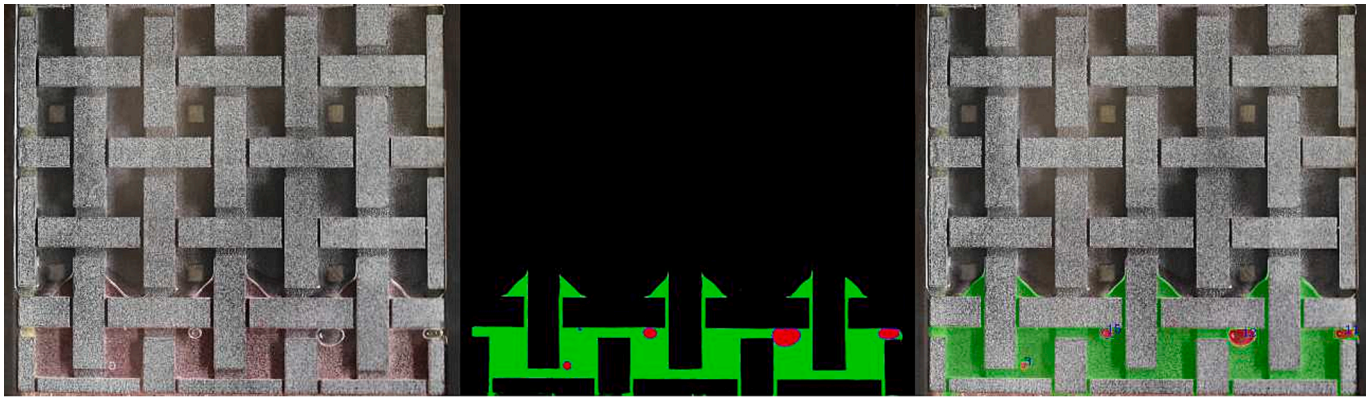

Fig. 4. (a) original video frame; (b) CNN segmentation by flowfront (green), bubble centroid (red) and bubble edge (blue) (c) superposition of segmentation map on the original frame and attribution of bubble ids. (For interpretation of the references to colour in this figure legend, the reader is referred to the web version of this article.)

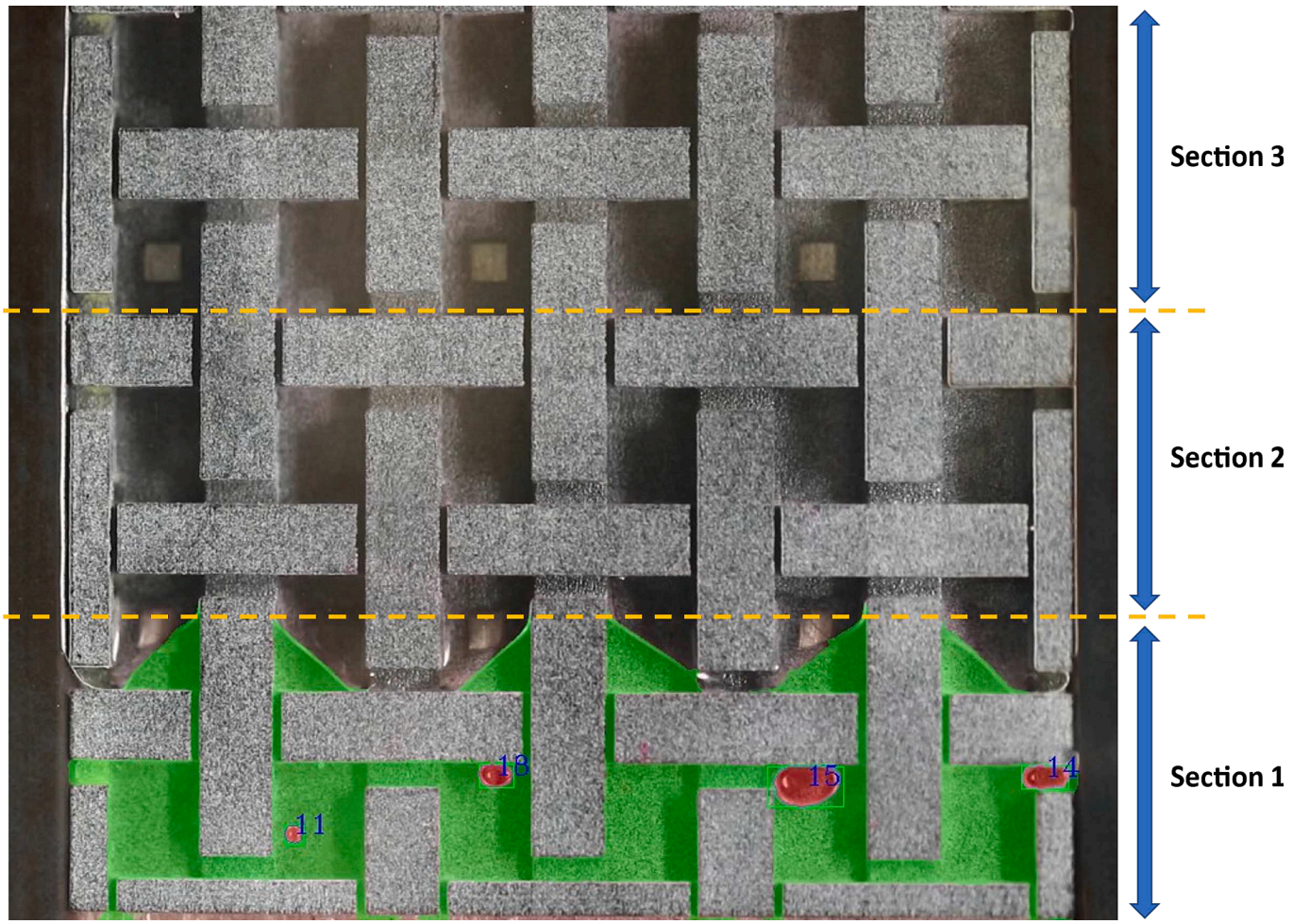

Fig. 5. Frame sections for the bubble velocity calculations.

calculation has negligible influence on the velocity calculations. The same principle applies to the flow-front velocity calculations.

The uncertainty regarding bubble volume variation due to the flow pressure gradient was also studied. Since the experimental setup did not encompass pressure sensors, the pressure gradient throughout the porous medium was estimated using Darcy's law (Eq. (1)), taking the permeability and porosity (∅) of the porous medium as listed in Table 2 [31] and the apparent flow velocity measured from the experiments. Following the relation in Eq. (6) based on the ideal gas law for isothermal compression or expansion, where p_1 is the pressure in the beginning of the porous medium, V_1 is the bubble volume after formation at the beginning of the porous medium, V_2 is the bubble volume at the end of the porous medium, p_2 is the pressure at the end of the porous medium (assumed to be the atmospheric pressure), $\partial p/\partial l$ is the pressure gradient parallel to the flow direction and Δl is the length of the porous medium, it is possible to predict the maximum bubble volume increase during the experiment.

$$\frac{V_2}{V_1} = \frac{p_2 - \frac{\partial p}{\partial l}\Delta l}{p_2} \tag{6}$$

The maximum expected bubble volume increase is approximately 9 % for experiments with the SLA printed porous medium, at a capillary number of 0.0296, which considering a spherical bubble would equate to a radius increase of 2.9 %. This upper limit of volume increase is only achieved if the bubble traverses the entire porous medium, which would require the bubble to be formed in the beginning of the porous medium. In turn, as bubbles are formed due to the flow front advancement throughout the porous medium length, the volume increase experienced by most bubbles during the experiments is expected to be very small.

Table 2
Permeability and porosity of the porous medium.

K_{xx}(small gap direction)	K_{yy} (large gap direction)	∅
3.28e-9 m^2	3.4e-8 m^2	59 %

3. Results and discussion

3.1. Void metrics

As can be seen from Fig. 3, as the flow front advances from the inlet towards the outlet, it merges trapping the air in between and forming bubbles of different sizes. These bubbles move with the fluid towards the outlet at different velocities. As the flow front progressed from the inlet to the outlet, bubble density and distribution was analysed counting the number of bubbles generated, total bubble area (which is the sum of all individual bubble areas) and bubble size distribution. Thus, this also allows a macro-level characterization of the behaviour of bubble formation and transport.

Regarding the number of generated bubbles during the flow experiment, data suggests that the number of bubbles has a positive correlation with the capillary number, as depicted in Fig. 6. It can also be observed that the architecture of the porous medium influences the number of generated bubbles, as the flow experiments using the orientation of the porous medium containing smaller gaps generate more

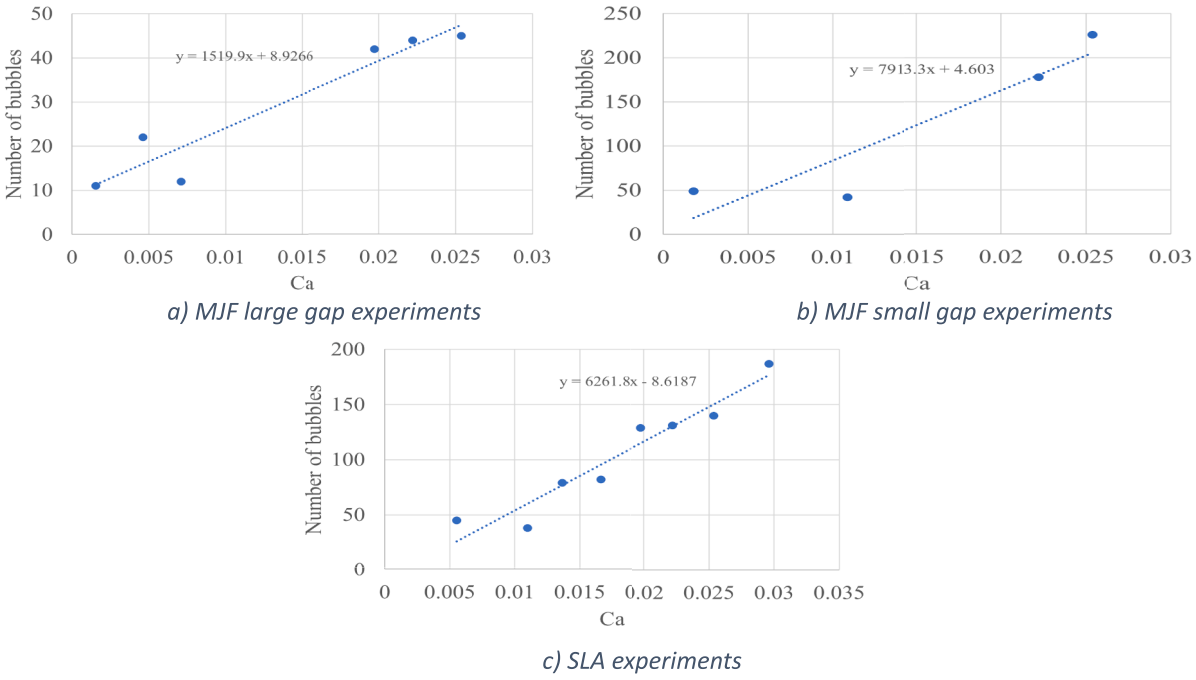

Fig. 6. Number of bubbles vs flowrate: a) MJF large gap experiments, b) MJF small gap experiments, c) SLA experiments.

bubbles than experiments using the large gap direction.

Moreover, comparing the number of generated bubbles in the MJF small gap experiments and the SLA experiments a difference in the number of generated bubbles is noticeable. A possible explanation for this effect may be attributed to the surface roughness of the porous media, which is significantly higher in the MJF printed medium (approximately three times higher compared to SLA) [39]. This increased surface roughness can trap tiny pockets of air in surface crevices and also favour the nucleation of bubbles during the flow of fluid from inlet to the outlet [40].

The total bubble area, calculated as the sum of all individual areas of the bubbles generated throughout the experiment, presents a V-shaped profile as also confirmed by [41] (Fig. 7 a to c), with a minimum achieved around a capillary number of ~ 0.01. This optimum capillary number, corresponding to the minimum bubble formation, has been found to be in agreement with the literature, as it has values of the same order of magnitude reported by [31] and [33] using real textile reinforcements. Nevertheless, it is reported that the existence of an

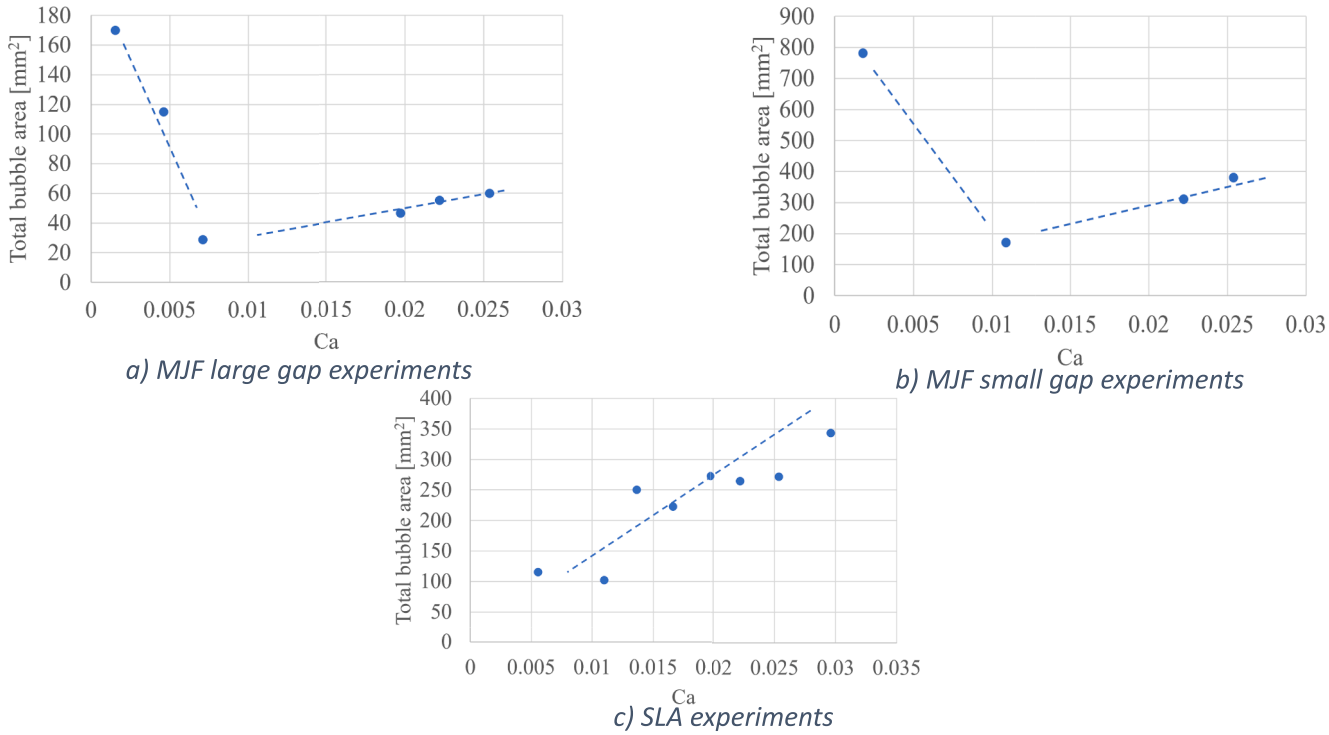

Fig. 7. Total bubble area vs capillary number: a) MJF big gap experiments, b) MJF small gap experiments, c) SLA experiments.

optimum capillary number is due to the balance between the generation of *meso*-scale voids (bubbles between the tows) and micro-scale voids (bubbles inside the tows) [20,43]. This is attributed to the flow front lead-lag effect, created by the competition between the capillary pressure driving the flow inside the tows, and the hydrodynamic pressure driving the flow in between the tows. In turn, for an increasing capillary number past the optimum, as the hydrodynamic pressure is the main driving mechanism, the bubbles should form inside the tows resulting in very low *meso*-scale void content. In our experiments this is not observed, as the reference porous medium possesses solid tows, which makes it a single scale porous medium. Consequently, in our experiments the increase of the capillary number tends to generate smaller bubbles as shown using boxplots in Fig. 8 to Fig. 10, totalling a higher number, as explained earlier. Although the mechanisms responsible for the formation of smaller bubbles with increasing capillary number are still unclear, this balance between bubble size and number of bubbles is what results in the V-shaped profile. An important observation to note is the absence of a V-shaped profile in the SLA porous medium data (Fig. 7c). One possible explanation for the formation of the V-shaped profile in Fig. 7a and 7b could be the nature of the 3D-printed Multi Jet Fusion (MJF) techniques. In MFJ technique, particle sintering is the main mechanism of layer formation and hence it may still leave behind capillary spaces among the particles while the SLA selectively cures and solidifies the photopolymer resin [3132] Hence SLA printing has much smoother surfaces than MJF parts. However, the conventional understanding involving capillary spaces in the MJF media may not entirely explain this phenomenon. Another consideration is that there might indeed be a V-shape in the SLA curve, but the tested capillary numbers (Ca) are too high to observe the left side. This speculation suggests that examining lower Ca values might reveal a different trend. Furthermore, Fig. 10 demonstrates a higher level of consistency in bubble area compared to Figs. 8 and 9. This could potentially be attributed to smoother media, provided the outliers on the right are excluded from consideration. These insights prompt a need for further investigation into the relationship between capillary spaces, capillary numbers, and void formation in both SLA and MJF processes.

3.2. Void transport metrics

Using the Buckingham π theorem, it was possible to reduce the number of parameters by forming different dimensionless groups.

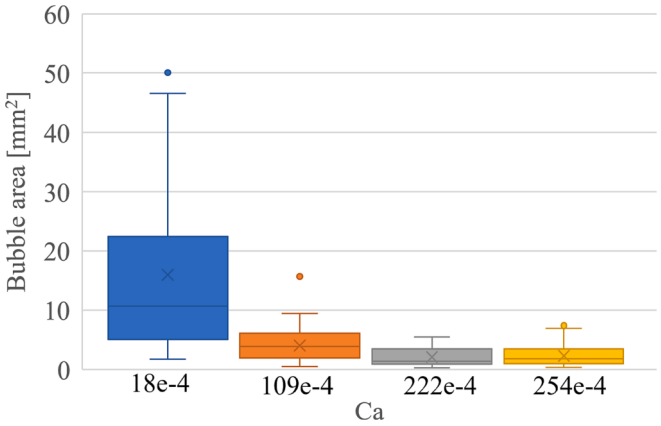

Fig. 9. Boxplot showing the minimum and maximum values along with median, first and third quartile of individual bubble areas vs capillary number for MJF small gap experiments. The outliers are shown as dots.

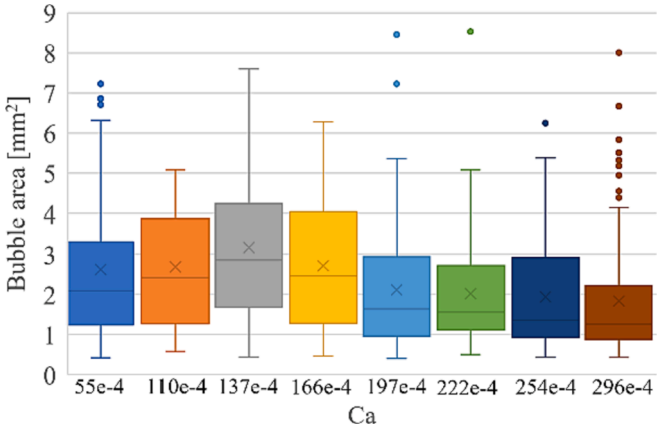

Fig. 10. Boxplot showing the minimum and maximum values along with median, first and third quartile of individual bubble areas vs capillary number for SLA experiments. The outliers are shown as dots.

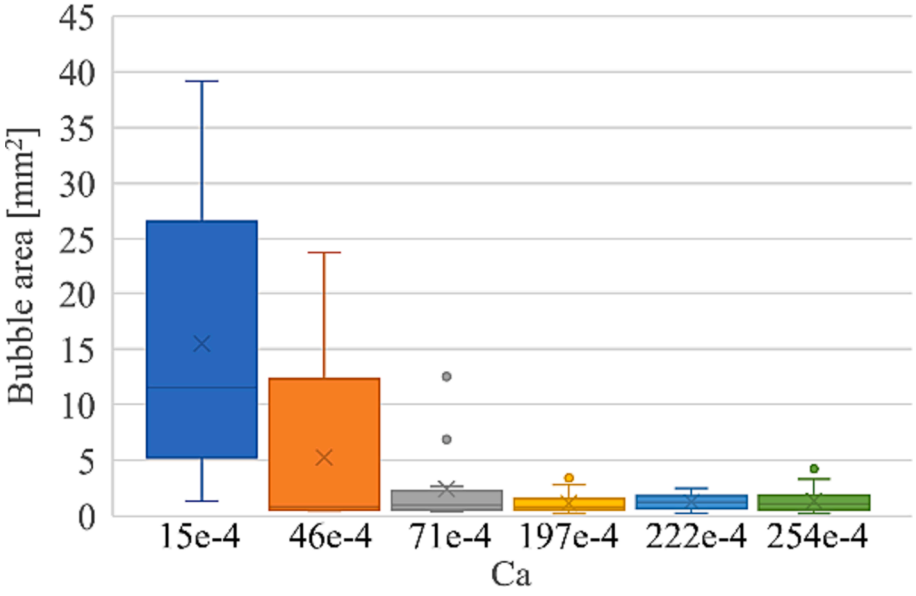

Fig. 8. Boxplot showing the minimum and maximum values along with median, first and third quartile of individual bubble areas vs capillary number for MJF large gap experiments. The outliers are shown as dots.

The variables taken into consideration are the average fluid velocity (v_{fl}), the bubble velocity (v_b), the fluid surface tension (σ), the fluid viscosity (μ), the bubble diameter (d_b) and the hydraulic diameter of the gaps that are aligned in the flow direction (d_g). The hydraulic diameter of the gaps was calculated according to Eq. (7), where A_g is the cross-section area and P_g is the wetted perimeter of the gap. The diameter of each bubble was calculated from its area (A_b), using Eq. (8). The area considered in the diameter calculations for each bubble, corresponds to the average of its history recorded by the algorithm.

$$d_g = \frac{4A_g}{P_g} \tag{7}$$

$$d_b = \sqrt{\frac{A_b}{\pi}} \tag{8}$$

The list of the considered variables and corresponding dimensions are presented in Table 3.

Considering a total of six variables and the three dimensions, three dimensionless groups were obtained:

$$\pi_1 = \frac{v_b}{v_{fl}} = M_b \tag{9}$$

$$\pi_2 = \frac{d_b}{d_g} = S_b \tag{10}$$

$$\pi_3 = \frac{v_{fl}\mu}{\sigma} = Ca \tag{11}$$

The first dimensionless group π_1 represents the bubble mobility. Bubble mobility (M_b) can be described as the relative velocity of the bubble, considering the apparent velocity of the flow inside the porous medium (v_{fl}) [44]. This parameter is of interest in this study, as it has been used in previous studies as a reference parameter to estimate bubble velocity [45,46]. The second dimensionless group π_2 consists of the quotient between the bubble diameter and the gap hydraulic diameter. For this study, it was taken as the bubble dimensionless size (S_b), which acts as a geometrical parameter. The third dimensionless group π_3 represents the capillary number (Ca).

From the obtained dimensionless groups, it is possible to infer that bubble mobility is a function of both geometrical conditions, given by the bubble dimensionless size (S_b), and the fluid flow conditions, given by the capillary number (Ca).

$$M_b = f(S_b, Ca) \tag{12}$$

3.3. Effect of capillary number on bubble mobility

The first objective was to study the effect of capillary number on bubble mobility. From the boxplots presented in Fig. 11 to Fig. 13, one may conclude that capillary number alone seems to have a small effect on bubble mobility. On the other hand, the capillary number does not seem to have a significant influence on bubble mobility, on MJF large gap experiments. This behaviour has been observed in the literature [47], where for small capillary numbers, the capillary number alone did not play a strong role in bubble mobility through the reinforcing porous

Table 3
Variables and Dimensions of the considered problem.

Variables	Dimensions
v_{fl}	LT^{-1}
$v_{b\sigma}$	$L\,T^{-1}$
σ	MT^{-2}
μ	$ML^{-1}\,T^{-1}$
d_b	L
d_g	L

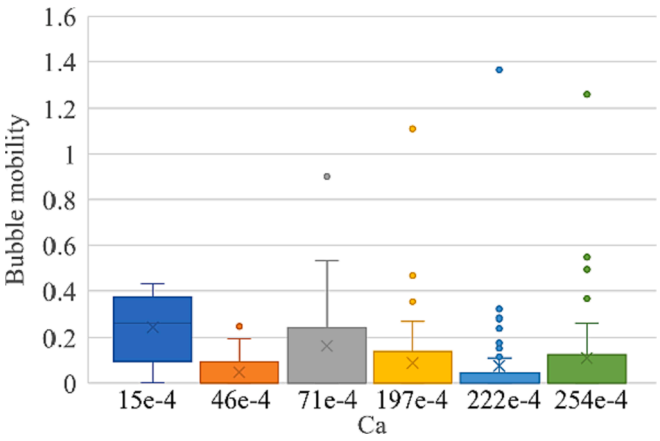

Fig. 11. Boxplots of bubble mobility vs capillary number for MJF large gap experiments.

medium. Nevertheless, the study also points out that in order for bubbles to move, a positive capillary number is in fact needed. Therefore, it is reasonable to assume that while not predominant, Ca does play a role in bubble mobility and as such, it should be incorporated as a parameter in models addressing bubble mobility.Fig. 12..

It can be observed that bubble mobility values are more concentrated in values between 0.5 and 1.0, whereas the boxplot whiskers with mobility above unity usually refer to bubbles which coalesce with the flow front. Also, there are bubbles which are a product of a bubble split before a porous media constriction and soon after coalesce with another bubble positioned ahead of the constriction. Since these bubbles' lifetime is restricted to local high flow velocity zones (near porous media constrictions), their computed mobility is higher than unity. This phenomenon is more predominant in higher flow rates, which is visible by the prolonged boxplot whiskers and higher number of outliers.

These results contrast with bubble mobility research based on microfluidics and Bretherton's theory [25,48], which reports that the velocity of the bubble is always higher than the average velocity of the flow and monotonically increases with the capillary number, for capillary numbers relevant to LCM processes. However, the use of a porous architecture introduces several conditions that are not present in capillary tubes, such as a more complex flow velocity field, as the cross section varies depending on the position within the porous medium. Moreover, the solid tows act as obstacles for the bubble paths, slowing down or stalling bubble movement, and increasing the length of the tortuous path, which does not happen in capillary tubes (Fig. 14). In turn, it is plausible that a higher dispersion of mobility values,

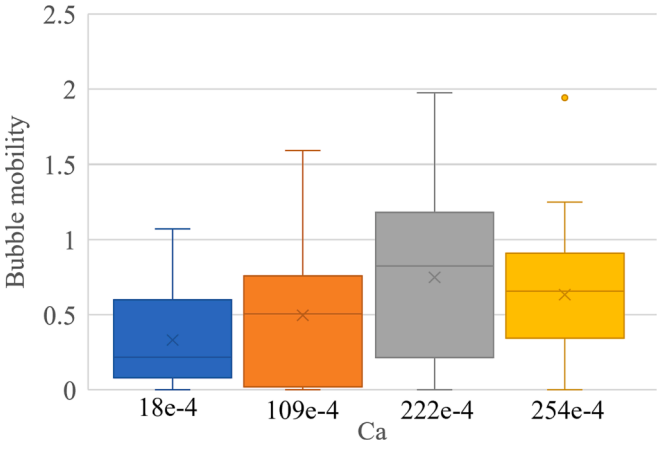

Fig. 12. Boxplots of bubble mobility vs capillary number for MJF small gap experiments.

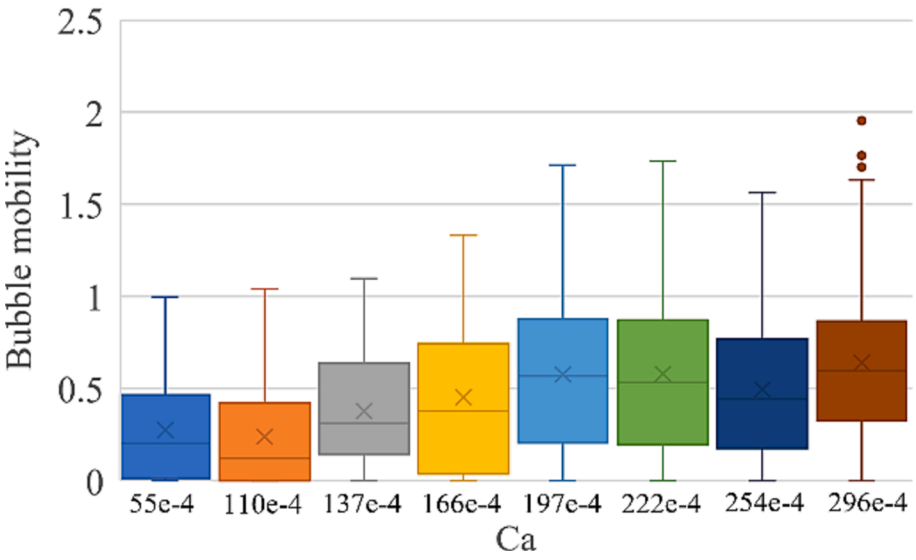

Fig. 13. Boxplots of bubble mobility vs capillary number for SLA experiments.

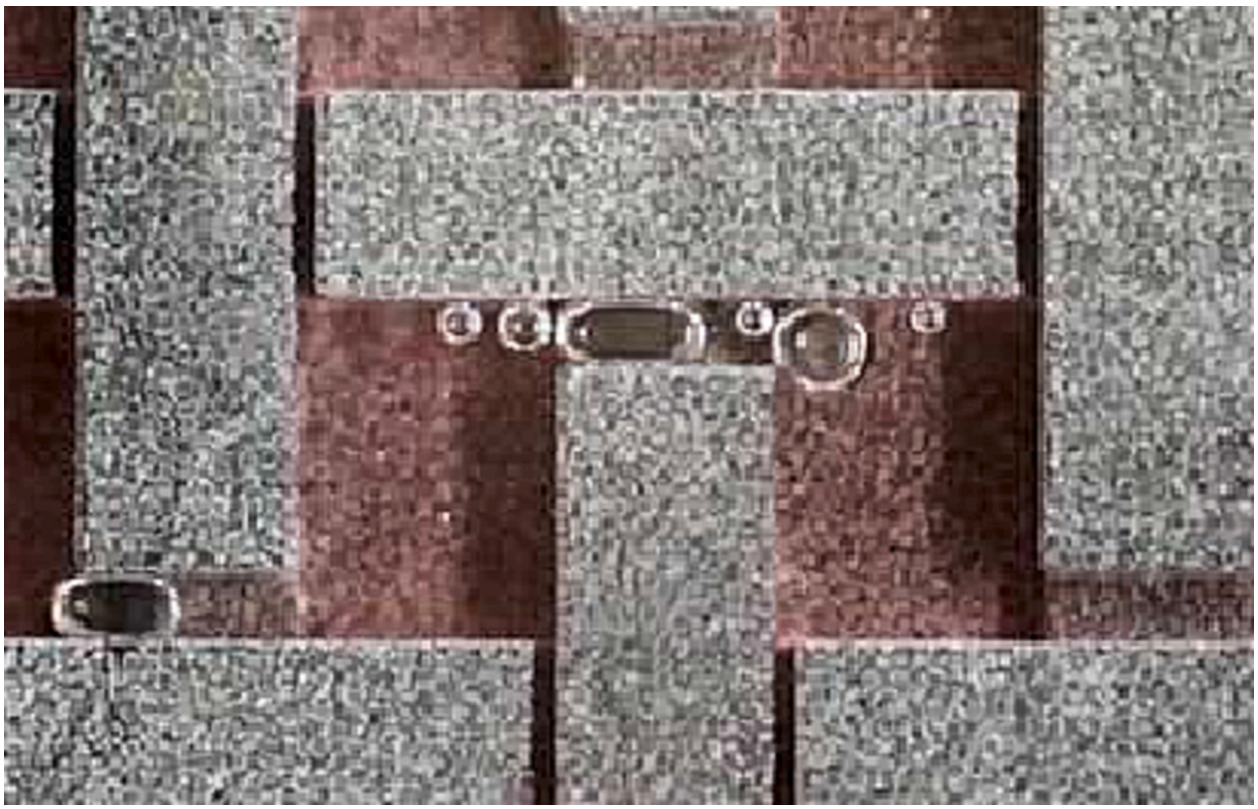

Fig. 14. Example of immobile bubbles due to porous medium blockage.

translating to a lower overall bubble mobility should be expected using the current setup, as compared to capillary tubes. This has been observed in experiments using porous geometries [28], in which the mobility of bubbles can drop below unity. Consequently, it has been suggested in the literature that the capillary number alone is not appropriate to describe bubble mobility, thus a new dimensionless number considering the geometrical properties of the bubble and the porous medium needs to be formulated [28].

3.4. *Effect of bubble size on bubble mobility*

The effect of dimensionless bubble size on bubble mobility was also analysed, by correlating each bubble average mobility with its dimensionless size. From Fig. 15 it can be observed that the influence of bubble dimensionless size on bubble mobility is twofold: for bubble diameters smaller than the gap hydraulic diameter, bubble mobility tends to increase. On the other hand, for bubble diameters larger than the gap hydraulic diameter, bubble mobility tends to decrease with bubble dimensionless size. The inflexion point between these two opposite tendencies is when the bubble diameter is approximately equal to the

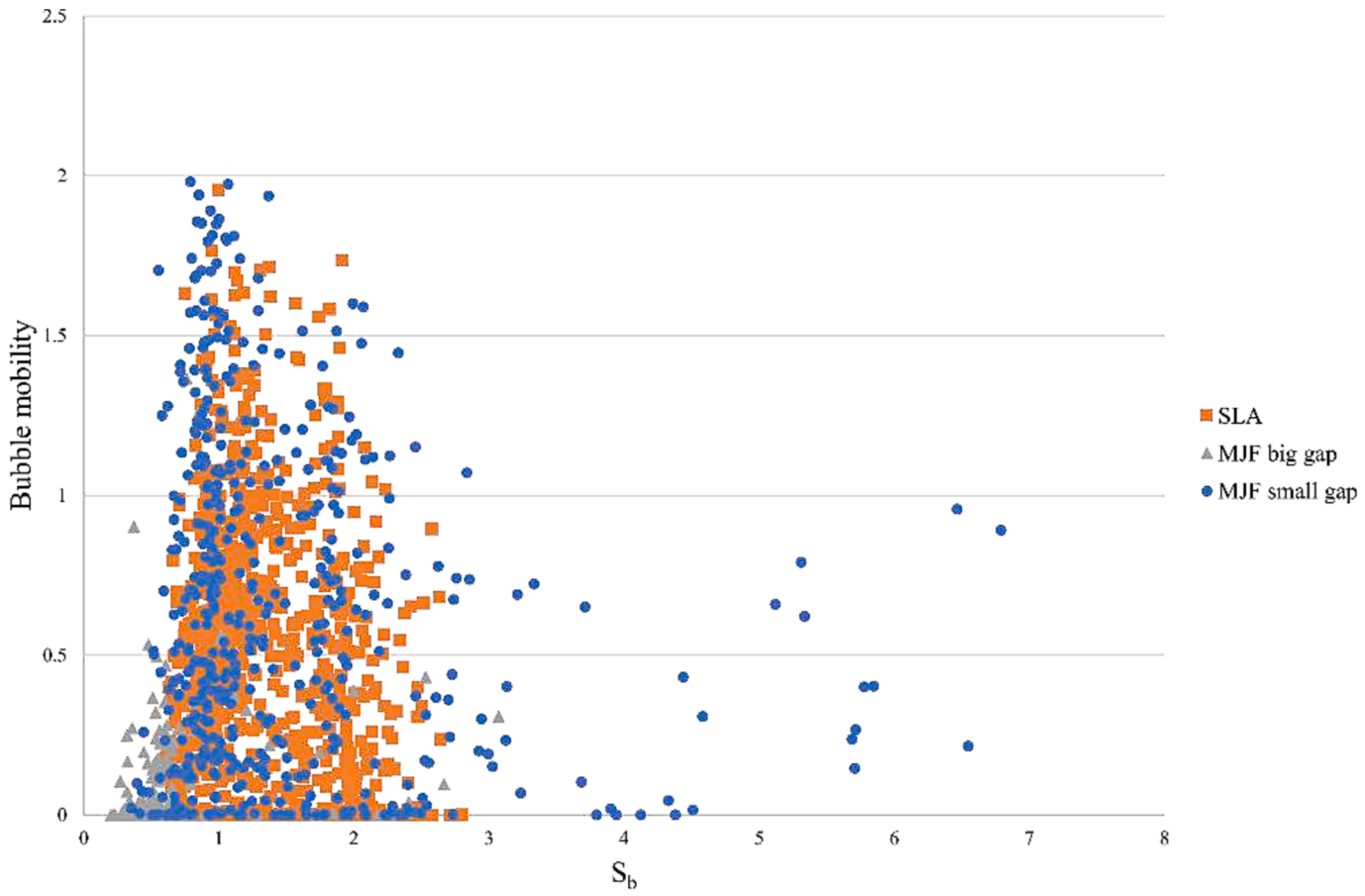

Fig. 15. Scatterplot of bubble mobility vs bubble dimensionless size.

gap hydraulic diameter. On a qualitative level, these results agree well with the theory. Considering the bubbles to be approximately spherical, the forces promoting a higher bubble mobility are the Stokes drag and the force due to the pressure gradient, as expressed in Eq. (13):

$$F = 3\pi\mu d_b\left(v_f - v_b\right) - \frac{\pi}{6}d_b^3\nabla p \tag{13}$$

where μ is the fluid viscosity, v_f is the fluid velocity, v_b is the bubble velocity, d_b is the bubble diameter and ∇p is the pressure gradient.

This means that the forces increase with the bubble diameter, by which a higher mobility should be expected as bubbles get bigger. Hence, the obtained results for bubbles with diameter smaller or equal to the gap hydraulic diameter agree with theory, as bubble mobility increases with bubble diameter. On the other hand, for bubbles which diameter is larger than the gap hydraulic diameter, additional work must be done to squeeze the bubble through the narrower gap. This additional work is due to the deformation the bubble experiments while traversing the gap, which is counteracted by the surface tension. The required pressure differential for mobilizing a bubble through a constriction, derived from the work principle, was found to be dependent on both the bubble diameter and the constriction diameter, as denoted in Eq. (14) [49].

$$\Delta p = 4\sigma\left(\frac{1}{d_c} - \frac{1}{d_b}\right) \tag{14}$$

Where Δp is the pressure differential, σ is the surface tension, d_c is the constriction diameter and d_b is the bubble diameter.

Based on Eq. (14), as bubble size increases, a higher-pressure differential is necessary to overcome the force generated by the deformation of the bubble. Once again, the experimental results are corroborated by theory, as bubble mobility decreases with bubble size, for bubbles with diameter larger than the gap hydraulic diameter. The decrease in mobility is based on the increase of the force generated by the deformation of the bubble, over the forces enumerated in Eq. (13). This type of behaviour has also been observed in other experimental studies regarding void transport in porous like structures [28].

4. Conclusions

In this study, void dynamics (formation and transport) in the context of Liquid Composite Moulding were studied using two calibrated textile-like porous media manufactured by Stereolithography and Multi Jet Fusion 3D printing technologies. By recording the unsteady two-phase flow mould filling flow experiments it was possible to capture void formation and their mobility inside the porous medium during the filling process. The use of a machine learning based algorithm developed to the effect, enabled the post-processing of the experimental recordings, leading to new conclusions regarding void dynamics, namely the statistical characterization of void mobility.

Results suggest that there is an optimum capillary number, which minimizes overall void content. This is the outcome of the balance between the number of bubbles generated, which has a positive correlation with the capillary number, and their respective size, which has a negative correlation with the capillary number.

Future work will be conducted with real dual-scale fibrous preforms, to assess how the differences in the porous medium geometry will affect the mesoscopic fluid flow and bubble mobility. Numerical simulations will be combined with experimental results to obtain correlations with local flow conditions.

CRediT authorship contribution statement

João Machado: . **Masoud Bodaghi:** Conceptualization, Data curation, Formal analysis, Methodology, Resources, Software, Supervision, Visualization, Writing – original draft, Writing – review & editing. **Mostafa Nikzad:** Methodology, Resources, Visualization, Writing – review & editing. **Pedro P. Camanho:** . **Suresh Advani:** Methodology, Writing – review & editing. **Nuno Correia:** .

Declaration of competing interest

The authors declare that they have no known competing financial interests or personal relationships that could have appeared to influence the work reported in this paper.

Data availability

Data will be made available on request.

Acknowledgement

J. Machado acknowledges the support from the Associated Laboratory for Energy, Transports and Aeronautics (LAETA) under the Research Grant UIDB/50022/2020. M. Bodaghi acknowledges the support from the Luxembourg National Research Fund (FNR) for funding Structural composite material, NATALINA under the research grant INTER/MERA/19/13991124 in frame of M-ERA.Net.. M. Nikzad greatly appreciates the support of Eric Choi, Andrew Tarlinton and Colin Dingfelder from Swinburne AMDC and MPDE departments for 3D printing specimen. S. Advani gratefully acknowledges the funding provided by the NSF Award No.2023323.

References

[1] Murray RE, Snowberg D, Berry D, Beach R, Rooney S, Swan D. Manufacturing a 9-Meter Thermoplastic Composite Wind Turbine Blade 2017.
[2] Ó Máirtín P, McDonnell P, Connor MT, Eder R, Ó Brádaigh CM.. Process investigation of a liquid PA-12/carbon fibre moulding system. Compos Part A Appl Sci Manuf 2001;32:915–23. https://doi.org/10.1016/S1359-835X(01)00005-7.
[3] Bodaghi M, Costa R, Gomes R, Silva J, Correia N, Silva F. Experimental comparative study of the variants of high-temperature vacuum-assisted resin transfer moulding. Compos A 2020;129:105708. https://doi.org/10.1016/j.compositesa.2019.105708.
[4] Bodaghi M, Cristóvão C, Gomes R, Correia NC. Experimental characterization of voids in high fibre volume fraction composites processed by high injection pressure RTM. Compos Part A Appl Sci Manuf 2016;82:88–99. https://doi.org/10.1016/j.compositesa.2015.11.042.
[5] Mills AR. Jones J Investigation, manufacture, and testing of damage-resistant airframe structures using low-cost carbon fibre composite materials 2009;224:489–97. https://doi.org/10.1243/09544100JAERO573.
[6] Witik RA, Gaille F, Teuscher R, Ringwald H, Michaud V, Månson JAE. Economic and environmental assessment of alternative production methods for composite aircraft components. J Clean Prod 2012;29–30:91–102. https://doi.org/10.1016/j.jclepro.2012.02.028.
[7] Jacques K, Bax L, Vasiliadis H, Magallon I, Ong K. Polymer composites for automotive sustainability. 2015.
[8] Kardos JL, Duduković MP, Dave R. Void growth and resin transport during processing of thermosetting —. Matrix composites 1986:101–23. https://doi.org/10.1007/3-540-16423-5_13.
[9] Staffan Lundström T, Frishfelds V, Jakovics A. Bubble formation and motion in non-crimp fabrics with perturbed bundle geometry. Compos Part A Appl Sci Manuf 2010;41:83–92. https://doi.org/10.1016/j.compositesa.2009.05.012.
[10] Parnas RS, Salem AJ, Sadiq TAK, Wang H-P, Advani SG. The interaction between micro- and macro-scopic flow in RTM preforms. Compos Struct 1994;27:93–107. https://doi.org/10.1016/0263-8223(94)90071-X.
[11] Kermani NN, Simacek P, Advani SG. Porosity predictions during co-cure of honeycomb core prepreg sandwich structures. Compos Part A Appl Sci Manuf 2020;132:105824. https://doi.org/10.1016/j.compositesa.2020.105824.
[12] Mehdikhani M, Gorbatikh L, Verpoest I, Lomov S, v.. Voids in fiber-reinforced polymer composites: A review on their formation, characteristics, and effects on mechanical performance. J Compos Mater 2019;53:1579–669. https://doi.org/10.1177/0021998318772152.
[13] Naganuma T, Naito K, Kyono J, Kagawa Y. Influence of prepreg conditions on the void occurrence and tensile properties of woven glass fiber-reinforced polyimide composites. Compos Sci Technol 2009;69:2428–33. https://doi.org/10.1016/j.compscitech.2009.06.012.
[14] Huang H, Talreja R. Effects of void geometry on elastic properties of unidirectional fiber reinforced composites. Compos Sci Technol 2005;65:1964–81. https://doi.org/10.1016/j.compscitech.2005.02.019.
[15] Stamopoulos AG, Tserpes KI, Prucha P, Vavrik D. Evaluation of porosity effects on the mechanical properties of carbon fiber-reinforced plastic unidirectional laminates by X-ray computed tomography and mechanical testing. J Compos Mater 2016;50:2087–98. https://doi.org/10.1177/0021998315602049.
[16] Darcy H. Les fontaines publiques de la ville de Dijon. Paris: Dalmont; 1856.
[17] Šimáček P, Advani SG. Desirable features in mold filling simulations for liquid composite molding processes. Polym Compos 2004;25:355–67. https://doi.org/10.1002/pc.20029.
[18] Bodaghi M, Lomov SV, Simacek P, Correia NC, Advani SG. On the variability of permeability induced by reinforcement distortions and dual scale flow in liquid composite moulding: A review. Compos Part A Appl Sci Manuf 2019;120:188–210. https://doi.org/10.1016/j.compositesa.2019.03.004.
[19] Park CH, Woo L. Modeling void formation and unsaturated flow in liquid composite molding processes: a survey and review. J Reinf Plast Compos 2011;30:957–77. https://doi.org/10.1177/0731684411411338.
[20] Rohatgi V, Patel N, James LL. Experimental investigation of flow-induced microvoids during impregnation of unidirectional stitched fiberglass mat. Polym Compos 1996;17:161–70. https://doi.org/10.1002/pc.10601.
[21] Zingraff L, Michaud V, Bourban P-E, Månson J-A-E. Resin transfer moulding of anionically polymerised polyamide 12. Compos Part A Appl Sci Manuf 2005;36:1675–86. https://doi.org/10.1016/j.compositesa.2005.03.023.
[22] Leclerc JS, Ruiz E. Porosity reduction using optimized flow velocity in Resin Transfer Molding. Compos Part A Appl Sci Manuf 2008;39:1859–68. https://doi.org/10.1016/j.compositesa.2008.09.008.
[23] Shih CH, Lee LJ. Analysis of void removal in liquid composite molding using microflow models. Polym Compos 2002;23:120–31. https://doi.org/10.1002/pc.10418.
[24] Lundstrom TS. Bubble transport through constricted capillary tubes with application to resin transfer molding. Polym Compos 1996;17:770–9. https://doi.org/10.1002/pc.10669.
[25] Ben Abdelwahed MA, Wielhorski Y, Bizet L, Bréard J. Characterisation of bubbles formed in a cylindrical T-shaped junction device. Chem Eng Sci 2012;76:206–15. https://doi.org/10.1016/j.ces.2012.04.025.
[26] Fernberg SP, Sandlund EJ, Lundström TS. Mechanisms controlling particle distribution in infusion molded composites. J Reinf Plast Compos 2006;25:59–70. https://doi.org/10.1177/0731684406055455.
[27] Wielhorski Y, Ben AA, Bréard J. Theoretical Approach of Bubble Entrapment Through Interconnected Pores: Supplying Principle. Transp Porous Media 2013;96:105–16. https://doi.org/10.1007/s11242-012-0076-z.
[28] Kang K, Koelling K. Void transport in resin transfer molding. Polym Compos 2004;25:417–32. https://doi.org/10.1002/pc.20035.
[29] Pillai KM. Modeling the Unsaturated Flow in Liquid Composite Molding Processes: A Review and Some Thoughts. J Compos Mater 2004;38:2097–118. https://doi.org/10.1177/0021998304045585.
[30] Bodaghi M, Vanaerschot A, Lomov SV, Correia NC. On the variability of mesoscale permeability of a 2/2 twill carbon fabric induced by variability of the internal geometry. Compos Part A Appl Sci Manuf 2017;101:394–407. https://doi.org/10.1016/j.compositesa.2017.05.030.
[31] Bodaghi M, Ban D, Mobin M, Park CH, Lomov SV, Nikzad M. Additively manufactured three dimensional reference porous media for the calibration of permeability measurement set-ups. Compos Part A Appl Sci Manuf 2020;139:106119. https://doi.org/10.1016/j.compositesa.2020.106119.
[32] Bodaghi M, Mobin M, Ban D, Lomov S, v., Nikzad M.. Surface quality of printed porous materials for permeability rig calibration. Mater Manuf Process 2021;00:1–11. https://doi.org/10.1080/10426914.2021.1960994.
[33] Antonelli D, Farina A. Resin transfer moulding: mathematical modelling and numerical simulations. Compos Part A Appl Sci Manuf 1999;30:1367–85. https://doi.org/10.1016/S1359-835X(99)00044-5.
[34] Machado J, Bodaghi M, Camanho P, Correia N, Advani S. A machine vision algorithm to detect bubbles during fluid flow with applicability to Liquid Composite Moulding Process. J Nondestr Eval n.d. Doi: Under review.
[35] Ronneberger O, Fischer P, Brox H. U-Net: Convolutional Networks for Biomedical Image Segmentation. Medical Image Computing and Computer-Assisted Intervention – MICCAI 2015, vol. 9351, 2015, p. 209–17. Doi: 10.1007/978-3-319-24574-4_25.
[36] Abadi M, Agarwal A, Barham P, Brevdo E, Chen Z, Citro C, et al. TensorFlow: Large-scale machine learning on heterogeneous systems 2015. Doi: 10.1080/09548980500300507.
[37] Bradski G. The OpenCV Library. Dr Dobb's Journal of Software Tools 2000.
[38] King DE. Dlib-ml: A machine learning toolkit. J Mach Learn Res 2009;10:1755–8.
[39] Bodaghi M, Mobin M, Ban D, Lomov SV, Nikzad M. Surface quality of printed porous materials for permeability rig calibration. Mater Manuf Process 2021;00:1–11. https://doi.org/10.1080/10426914.2021.1960994.
[40] Pereiro I, Fomitcheva Khartchenko A, Petrini L, Kaigala GV. Nip the bubble in the bud: A guide to avoid gas nucleation in microfluidics. Lab Chip 2019;19:2296–314. https://doi.org/10.1039/c9lc00211a.
[41] Ruiz E, Achim V, Soukane S, Trochu F, Bréard J. Optimization of injection flow rate to minimize micro/macro-voids formation in resin transfer molded composites. Compos Sci Technol 2006;66:475–86. https://doi.org/10.1016/j.compscitech.2005.06.013.
[43] Patel N, Lee LJ. Modeling of void formation and removal in liquid composite molding. Part II: Model development and implementation. Polym Compos 1996;17:104–14. https://doi.org/10.1002/pc.10595.

[44] Simacek P, Niknafs Kermani N, Advani SG. Coupled Process Modeling of Flow and Transport Phenomena in LCM Processing. Integr Mater Manuf Innov 2022;11:363–81. https://doi.org/10.1007/s40192-022-00268-1.
[45] Gangloff JJ, Daniel C, Advani SG. A model of two-phase resin and void flow during composites processing. Int J Multiph Flow 2014;65:51–60. https://doi.org/10.1016/j.ijmultiphaseflow.2014.05.015.
[46] Gangloff JJ, Hwang WR, Advani SG. Characterization of bubble mobility in channel flow with fibrous porous media walls. Int J Multiph Flow 2014;60:76–86. https://doi.org/10.1016/j.ijmultiphaseflow.2013.12.003.
[47] Gangloff JJ, Cender TA, Eskizeybek V, Simacek P, Advani SG. Entrapment and venting of bubbles during vacuum bag prepreg processing. J Compos Mater 2017;51:2757–68. https://doi.org/10.1177/0021998316676325.
[48] Bretherton FP. The motion of long bubbles in tubes. J Fluid Mech 1961;10:166. https://doi.org/10.1017/S0022112061000160.
[49] Lundström TS. Bubble transport through constricted capillary tubes with application to resin transfer molding. Polym Compos 1996;17:770–9. https://doi.org/10.1002/pc.10669.